

# An Inference and Learning Engine for Spiking Neural Networks in Computational RAM (CRAM)

HÜSREV CILASUN, SALONIK RESCH, ZAMSHED IQBAL CHOWDHURY, ERIN OLSON, MASOUD ZABIHI, ZHENGYANG ZHAO, THOMAS PETERSON, KESHAB PARHI, JIAN-PING WANG, SACHIN S. SAPATNEKAR, and ULYA KARPUZCU, University of Minnesota

Spiking Neural Networks (SNN) represent a biologically inspired computation model capable of emulating neural computation in human brain and brain-like structures. The main promise is very low energy consumption. Unfortunately, classic Von Neumann architecture based SNN accelerators often fail to address demanding computation and data transfer requirements efficiently at scale. In this work, we propose a promising alternative, an in-memory SNN accelerator based on Spintronic Computational RAM (CRAM) to overcome scalability limitations, which can reduce the energy consumption by up to  $164.1\times$  when compared to a representative ASIC solution.

## 1 INTRODUCTION

Spiking Neural Networks (SNN) are neural networks mimicking the impulse based neural transmission in the brain. Recently, as a computational model, SNNs have been emerged as biologically more realistic, yet tractable alternatives to artificial neural networks. Although there are topological similarities to a fully-connected neural network, the main difference lies in the *spike* event, an electrical discharge triggered by a series of chemical reactions. Spike trains coming from *presynaptic neurons* are processed in the *postsynaptic neuron*, which enables computational tasks such as classification to be performed in SNN.

As a biologically inspired computational model capable of emulating neural computation in human brain and brain-like structures [12, 23], inherent SNN architecture poses as an ideal computing medium for event-driven processing [24]. As a result, SNN can perform a variety of computational tasks with significantly lower power consumption, such as prosthetic brain-machine interface control [8] and speech recognition [28]. Recent efforts [14] focus on flexible and efficient hardware emulation of different biologically accurate SNN models, while others exploit the computational power resulting from the high number of relatively simpler neurons in SNNs. Low energy hardware SNN accelerators such as ODIN [11] try to minimize the energy per spiking operation. SNN hardware solutions include IBM’s TrueNorth [17], Intel’s Loihi [6], University of Manchester’s SpiNNaker [12], and Human Brain Project’s BrainScaleS [20]. Present highest number of spiking neurons in a hardware SNN implementation is 1 Billion real-time neurons in SpiNNaker [13], only a fraction of the average neuron count of 86 Billion in human brain [15].

Large-scale SNNs needed to perform useful computational tasks inevitably come with increased data access and parallelism demand which often exceeds capabilities of traditional hardware. When neuron count increases significantly, more space is required to store synaptic parameters. Data access and retrieval becomes a burden at the same time, mainly because any spiking information emerging in neurons should be accessible to all other neurons as an input. Various solutions based on traditional CMOS as well as emerging spintronic and resistive technologies are proposed to overcome this bottleneck [18]. For example, recent Magnetic Tunneling Junction (MTJ) based spintronic SNN accelerators [2, 21, 27] multiply weights by spike trains using MTJs in a crossbar setting. These and similar designs typically only address a single

---

Authors’ address: Hüsrev Cilasun, cilas001@umn.edu; Salonik Resch, resc0059@umn.edu; Zamshed Iqbal Chowdhury, chowh005@umn.edu; Erin Olson, olso6834@umn.edu; Masoud Zabihi, zabih003@umn.edu; Zhengyang Zhao, zhaox526@umn.edu; Thomas Peterson, pete9290@umn.edu; Keshab Parhi, parhi@umn.edu; Jian-Ping Wang, jpwang@umn.edu; Sachin S. Sapatnekar, sachin@umn.edu; Ulya Karpuzcu, ukarpuzc@umn.edu, University of Minnesota, Twin Cities, Minnesota.

Manuscript submitted to ACM

stage of SNN computation – i.e., weight multiplication by spike train. Flexibility is also a concern, as the SNN model as well as parameter resolution is hardwired. Spintronic (MTJ based) devices have also been proposed as analog SNN building blocks [31], however, analog implementations by construction suffer from process variability constraints [25].

Putting it all together, large scale SNN computations are massively parallel and induce high-intensity memory accesses for data retrieval. As a result, the energy consumption skyrockets at scale. This is why true in-memory computing substrates such as the recently proposed spintronic Computational RAM (CRAM) [26], which enable massively parallel and reconfigurable logic operations *in-situ* without compromising energy efficiency, represent especially promising platforms for SNN hardware, which form the focus of this paper. We will start our discussion with background information covering basics of CRAM and the SNN model in Section 2. Section 3 details the proposed SNN architecture based on CRAM. After quantitative evaluation in Section 4, we conclude the paper in Section 5.

## 2 BACKGROUND

After covering CRAM basics, we will continue with the feedforward Leaky Integrate-and-Fire SNN model in Section 2.2. Although only the feedforward model is useful for many computational tasks, applications such as brain simulation needs the parameters to be learned online. To this end, we also include pairwise Spike-Time Dependent Plasticity (STDP) learning algorithm for updating parameters during computation, as need be.

### 2.1 CRAM Basics

Essentially, CRAM [26] augments conventional spintronic memory arrays with compute capability, thereby enabling seamless memory access. As long as there is no computation, CRAM reduces to an ordinary memory. When computation is enabled, CRAM performs logic operations directly inside the memory array. Spin Torque Transfer (STT) and Spin-Hall Effect (SHE) or Spin-Orbit Torque (SOT) based CRAM variants exists [4, 19, 29, 30]. CRAM can perform one logic operation (Boolean gate) in a column at a time, but all (or a desired subset of) columns can perform the same operation in parallel. Each cell in a column can serve as an input or output to a Boolean gate. Logic operations are reconfigurable in time and space. At the same time, multiple CRAM arrays can perform the same computation (across all of their columns) in parallel.

CRAM’s main storage element is a Magnetic Tunneling Junction (MTJ), which comprises a fixed-polarity magnetic layer, a variable-polarity magnetic layer, and an insulating layer in between. When polarities of the magnetic layers (mis)match, the MTJ is in (Anti)Parallel-(A)P state which corresponds to logic (1) 0, exhibiting a (high) low resistance.

Cell structures for STT- and SHE-CRAM are provided in Figure 1(a) and 1(b), respectively. STT-CRAM features even and odd bitlines (BLE/O), which are used to sense (change) the state of the MTJ in read (write) mode. For logic operations, BLE/O is used determine which MTJ serves as an input or output. Logic lines (LL) connect input and output cells to perform Boolean operations. STT-CRAM also has wordlines (WL), which are used to select the rows for both memory and logic operations.

Specifically, in order to perform a logic gate in Figure 1(a), first the output MTJ is preset to a known logic value depending on the type of the gate. If inputs reside in even rows, the output should be in an odd row, and vice versa. By imposing a specific voltage difference between BLE and BLO, a current is induced through (a parallel connection of) inputs and the output in series. The magnitude and direction of this current depends on the voltage difference between BLE and BLO, which also is a function of the type of the gate to be performed. For a given voltage difference, the current through the output evolves as a function of the parallel equivalent resistance of the inputs, and may or may not be enough to switch the output state. This is the main principle behind how CRAM implements truth tables. If the combined current is high enough

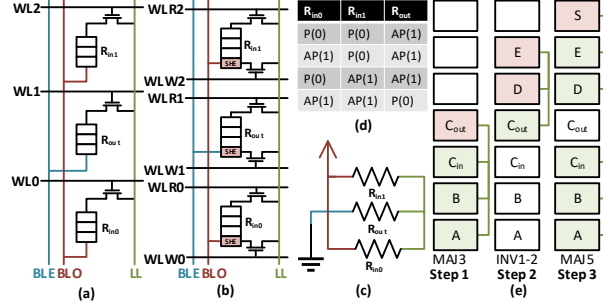


Fig. 1. (a) 1T1M STT-CRAM; (b) SHE-CRAM; (c) Equivalent resistive network for a NAND gate; (d) NAND truth table; (e) 3-step full adder implementation. MAJ3 and MAJ5 are 3-input and 5-input majority gates. INV1-2 is an inverter which writes the output to two different cells simultaneously.

to change the state of the output cell(s), the cell state is changed, effectively corresponding to the implementation of a logic gate. The equivalent resistive network for the universal NAND gate is given in Figure 1(c) along with the truth table in Figure 1(d). CRAM supports a rich set of (universal) gates beyond NAND, each characterized by specific bitline voltage and output preset values. More complex logic functions such as full-adders can be synthesized by a sequence of basic gate operations as shown in Figure 1(e) [3].

SHE-CRAM, as shown in Figure 1(b), on the other hand, features a four terminal cell element which enables faster memory and logic operations while consuming significantly less energy. This is because SHE-CRAM separates read and write paths, making independent optimization of each possible (which otherwise impose conflicting constraints). Accordingly, SHE-CRAM has separate read (WLR) and write (WLW) wordlines, and two access transistors per cell. SHE-CRAM hence has a higher area footprint compared to the STT-CRAM, which is compensated by lower energy and faster operation. Memory and logic operations follow the same principles otherwise.

To ease illustration, in the following, we will use *transposed* CRAM arrays, and abstract out the interleaved placement where inputs (outputs) reside in even (odd) rows or vice versa.

## 2.2 Leaky Integrate-and-Fire SNN Model

Although there exist more complex and biologically accurate models for SNNs, *Leaky Integrate-and-Fire* model, as described in [6], is widely used due to its relative simplicity. The general model assumes that each neuron is connected to *presynaptic neurons* which broadcast their own spike trains. Each connection from neuron  $j$  to neuron  $i$  is characterized by a weight  $\omega_{ij}$  and a delay value  $d_{ij}$  corresponding to the actual transmission delay in brain for more accurate modeling. Each spike train (or spike function) can be expressed as  $\sigma(t) = \sum_k \delta(t - t_k)$  where  $\delta$  is the unit impulse function;  $t$ , the discrete time variable; and  $t_k$ , the time difference corresponding to  $k^{th}$  spike. Table 1 provides the definition for all model parameters.

The weighted sum of filtered presynaptic spike trains with bias is called *synaptic response current*, as depicted in Equation (1), where  $u_i(t)$  represents the synaptic response current of neuron  $i$ :

$$u_i(t) = \sum_{j \neq i} \omega_{ij} (\alpha_u * \sigma_j)(t) + b_i \quad (1)$$

$\alpha_u(t) = \frac{1}{\tau_u} e^{-\frac{t}{\tau_u}} H(t)$  where  $H(t)$  is the unit step function;  $\tau_u$ , a time constant; and  $b_i$ , the bias.

Table 1. Parameter Definitions

Parameter	Definition
$t$	discretized time variable
$\sigma_j(t)$	spike train at the output of neuron $j$
$\tau_u$	neural time constant
$\tau_v$	synaptic time constant
$\theta_i$	spiking threshold constant of neuron $i$
$\omega_{ij}$	weight variable between neurons $i$ and $j$
$d_{ij}$	delay variable between neurons $i$ and $j$
$b_i$	bias variable of neuron $i$
$u_i(t)$	synaptic response current of neuron $i$
$v_i(t)$	membrane potential of neuron $i$
$A_{\pm}$	time constant
$t^{pre/post}$	presynaptic/postsynaptic spike time
$\alpha_u(t)$	$\frac{1}{\tau_u} e^{-\frac{t}{\tau_u}} H(t)$
$\mathcal{F}(t)$	$e^{-\frac{t}{\tau_u}} H(t)$
$L_f$	#entries in the lookup table of $\alpha_u(t)$
$S$	weight bit size
$t_{max}$	maximum time difference for STDP
$r(t)$	pseudorandom noise

The voltage difference between the inside and the outside of the synapse is called *membrane potential*. Update function for membrane potential is given as – where  $v_i(t)$  captures the membrane potential of neuron  $i$ :

$$v_i(t) = -\frac{1}{\tau_v} v_i(t) + u_i(t) - \theta_i \sigma_i(t) \quad (2)$$

$\tau_v$  here is a time constant;  $\theta_i$ , the threshold value for neuron  $i$ . If the neuron spikes,  $v_i$  is initialized to zero.

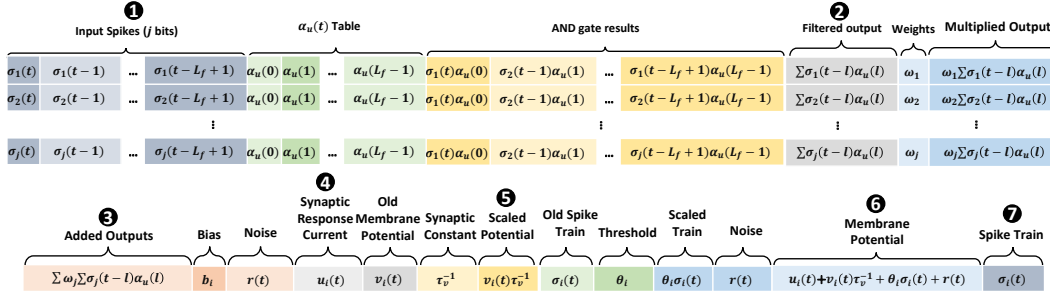


Fig. 2. Data layout (transposed).

Figure 3 depicts an overview of the model. Putting it all together, each neuron calculates its output spike train from presynaptic spike trains. Variations of this basic algorithm include the Random Sampling algorithm from Loihi [6], which our design is based on, and where synaptic response current and membrane potential are optionally incremented by a pseudorandom number – which we will encapsulate in the following discussion in a noise term  $r(t)$ .

### 2.3 Pairwise STDP based Parameter Learning

Learning entails adjusting synaptic weights ( $\omega_{ij}$ ) and delays ( $d_{ij}$ ) to dynamically optimize the neural network for solving a specific problem. It models the actual synaptic changes which brain adapts to accommodate new constraints.

STDP model features a simple weight learning rule, as described in [5, 6]. It can be summarized as follows

$$\Delta\omega_{i,j} = \begin{cases} A_- \mathcal{F}(t - t_i^{post}), & \text{on presynaptic spike} \\ A_+ \mathcal{F}(t - t_j^{pre}), & \text{on postsynaptic spike} \end{cases} \quad (3)$$

where  $\mathcal{F}(t) = e^{-\frac{t}{\tau}} H(t)$  and  $\tau$ ,  $A_-$ , and  $A_+$  are constants, as defined in Table 1.  $\Delta\omega_{i,j}$  is added to the weight in each update.

Figure 8 provides a block diagram description of the basic STDP algorithm. We define  $\Delta t^{pre(post)}$  as  $t - t_{j(i)}^{pre(post)}$ . The algorithm continuously checks whether the current neuron or a presynaptic neuron spikes. If so, it resets the  $\Delta t^{pre(post)}$  counter by multiplying its former value by zero. Otherwise, it checks for overflow and increments the  $\Delta t^{pre(post)}$ , which is then fed to  $\mathcal{F}(\cdot)$  function and multiplied by  $A_{+(-)}$ .

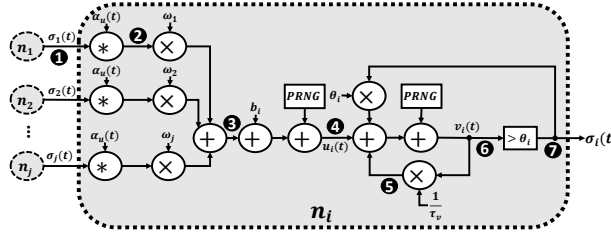


Fig. 3. Leaky Integrate-and-Fire model [6].

## 3 SNN IN CRAM

### 3.1 Leaky Integrate-and-Fire-Model in Memory

CRAM supports universal Boolean gates, hence can handle any type of computation including the Leaky Integrate-and-Fire Model described in Section 2.2. The mapping is straightforward, as shown in Figure 2, where each neuron gets processed inside a single CRAM array to exploit array-level parallelism.

Table 2. CRAM array utilization by constants, parameters, and lookup table for different  $S$  and  $L_f$ s.

$S$	$L_f$	Array Size	Utilization
1 – 4	32	$256 \times 256$	14.06% – 56.25%
5 – 8	32	$512 \times 512$	35.15% – 56.25%
9 – 16	32	$1024 \times 1024$	31.64% – 56.25%
1 – 2	64	$256 \times 256$	26.55% – 53.13%
3 – 4	64	$512 \times 512$	39.84% – 53.13%
5 – 8	64	$1024 \times 1024$	33.2% – 53.13%
9 – 16	64	$2048 \times 2048$	29.88% – 49.8%

**3.1.1 Initialization.** Our design incorporates several lookup tables (LUT) and dedicated storage for parameters and constants, which are initialized before feedforward computations start. The initialization is a one-time procedure, as the corresponding values do not change during computation. We also initialize an  $S$ -bit *local delay* value for each synapse, which serves modeling synaptic delays between neurons.

Precomputed  $\alpha_u$  values reside in a lookup table.  $\alpha_u$  lookup table consists of  $L_f$  different  $S$ -bit values (Table 1). Similarly, constant  $\frac{1}{\tau_v}$  is initialized once, as well as weights  $\omega_{ij}$ ,  $b_i$ , and  $\theta_i$  values. For the  $\alpha_u$  lookup table, Table 2 shows the utilization for different CRAM array sizes for various  $S$  and  $L_f$ . We choose the array size so that the utilization does not exceed approximately half of the array size. Thereby enough space is left to perform the arithmetic/logic operations in remaining CRAM space.

**3.1.2 Data Flow.** Once a spike train of presynaptic neurons is received, it is written in the memory as shown in the first column in Step ❶. Along with all the previously received (and similarly placed) spikes, these spikes and the  $\alpha_u(s)$  values are multiplied where  $s \in [0, L_f - 1]$  and  $L_f$  is the predetermined filter length. This filtering operation effectively corresponds to the convolution (\*) from Equation (1). Since all of the values involved are binary, this operation reduces to  $S \times L_f$  AND operations where  $S$  is the bit length of each entry in the  $\alpha_u(s)$  lookup table, which keeps precomputed values of the  $\alpha_u(s)$  function. Once ANDs are computed, the resulting  $L_f$  entries are added together and rounded (Section 3.1.3) to  $S$  bits to obtain the column denoted by ❷ in Figure 2. In order to prepare the spike train for the next spike computation cycle, the spike train is next shifted by reading the columns obtained in Step ❶ and writing them to another row. Then, the resulting  $S$  bit values are multiplied by  $S$  bit weights, which corresponds to  $S^2$  full adder operations and results in the column marked by Step ❸. The  $2S$  multiplication outcome is next rounded to  $S$  bits, i.e., a  $(S - 1)$ -bit rounding factor is added to it and the result is truncated to  $S$  bits. Addition is again performed as a cascade of full adder operations. Truncation has practically no overhead as it translates into simply ignoring the unused bits. Equation (1) gives rise to the operations we covered so far, spanning Step ❶ to Step ❸.

In the following step, all rows in Step ❸ are added by reading half of the rows and writing them back to the adjacent rows. After each addition, a rounding operation is performed. This operation takes  $\log_2 j$  stages where  $j$  is the predetermined maximum number of presynaptic neurons. Once the addition is done, the result is reduced to a single row as shown in Step ❹. After the bias and the noise is added to the outcome from Step ❹, synaptic response current shown in Step ❺ is obtained. We keep older membrane potential in the same row, which is next scaled – by multiplication with  $\tau_v^{-1}$ . Previous spike train is multiplied by the threshold value  $\theta$ , which reduces to an AND operation of  $S$  bits. Equation (2) spans Step ❹–Step ❻. The current membrane potential is obtained after current synaptic response current, scaled old membrane potential, the noise, and the scaled old spike train is added as shown in Step ❻. Current membrane potential then overwrites the old membrane potential. Finally, current spike value is calculated by thresholding the current membrane potential in Step ❼, which corresponds to the comparison of  $S$ -bits. Current spike value is written as shown in Step ❼ and copied to the old spike train column. In order to reset the membrane potential, we invert the spike bit and AND with the membrane potential. The output spike is then read and broadcasted as we will explain in Section 3.2.

Before starting computation, the  $S$ -bit local delay value in all columns is incremented and compared to  $d_{i,j}$  (for the corresponding synaptic connection). If the comparison yields true, the local delay value is reset to zero. The comparison output is then read by the array controller and used as column enable. This results in a practical synaptic delay implementation, as well as energy savings, as the disabled columns do not participate in computations described above to perform Equations (1) and (2).

**3.1.3 Low Level Operations.** For addition operations, we use the full adder from Figure 1. Multiplication also uses the same full adder design  $N^2$  times for  $N$ -bit numbers. In the convolution with  $\alpha_u(t)$ , the multiplications reduce to AND operations since the spikes are binary. Comparison by the threshold value is implemented as a cascade of  $6N - 3$  NAND gates for  $N$ -bit numbers. We increase the bit size conservatively until Step ③ and then we perform rounding operation by adding rounding factors in each arithmetic operation, which ensures that no overflow happens. Rounding to  $S$  bits entails adding a  $(S - 1)$  bit long rounding factor and then keeping only the  $S$  most significant bits.

Time	Memory Layout										Operation			
$t_n$	b1	b2	b3	b4	b5	b6	b7	b8	b9	t	a0	a1	a2	PRESET(t,a0,a1,a2)
$t_{n+1}$	b1	b2	b3	b4	b5	b6	b7	b8	b9	t	a0	a1	a2	NAND(b5,b9,a0)
$t_{n+2}$	b1	b2	b3	b4	b5	b6	b7	b8	b9	t	a0	a1	a2	NAND(b5,a0,a1)
$t_{n+3}$	b1	b2	b3	b4	b5	b6	b7	b8	b9	t	a0	a1	a2	NAND(b9,a0,a2)
$t_{n+4}$	b1	b2	b3	b4	b5	b6	b7	b8	b9	t	a0	a1	a2	NAND(a1,a2,t)
$t_{n+5}$	b1	b2	b3	b4	b5	b6	b7	b8	b9	t	a0	a1	a2	COPY(b8,b9)
$t_{n+6}$	b1	b2	b3	b4	b5	b6	b7	b8	b9	t	a0	a1	a2	COPY(b7,b8)
$t_{n+7}$	b1	b2	b3	b4	b5	b6	b7	b8	b9	t	a0	a1	a2	COPY(b6,b7)
$t_{n+8}$	b1	b2	b3	b4	b5	b6	b7	b8	b9	t	a0	a1	a2	COPY(b5,b6)
$t_{n+9}$	b1	b2	b3	b4	b5	b6	b7	b8	b9	t	a0	a1	a2	COPY(b4,b5)
$t_{n+10}$	b1	b2	b3	b4	b5	b6	b7	b8	b9	t	a0	a1	a2	COPY(b3,b4)
$t_{n+11}$	b1	b2	b3	b4	b5	b6	b7	b8	b9	t	a0	a1	a2	COPY(b2,b3)
$t_{n+12}$	b1	b2	b3	b4	b5	b6	b7	b8	b9	t	a0	a1	a2	COPY(b1,b2)
$t_{n+13}$	b1	b2	b3	b4	b5	b6	b7	b8	b9	t	a0	a1	a2	COPY(t,b1)

Fig. 4. Linear Feedback Shift Register (LFSR) based pseudorandom number generation in CRAM using feedback polynomial  $x^9 + x^5 + 1$ . Input (output) cells are highlighted with green (red).

Loihi [16] features a Pseudorandom Noise Generator (PRNG) to support several variants of the basic algorithm such as neural sampling. As a proof of concept, we demonstrate how to implement a PRNG in CRAM using a basic linear feedback shift register in Figure 4. First, an XOR gate is applied as a cascade of four NAND gates and then COPY operations are performed as many as the length of the feedback polynomial. For an example 9-bit polynomial, this operation takes 13 cycles. We denote this generated noise with  $r(t)$  and update each time it is used.

Our lookup table based implementation of  $\alpha_u(t)$  function and the inevitably limited bit length for parameters such as weights, by construction, affect synaptic accuracy. Section 4 provides a quantitative characterization of the accuracy impact of precision.

## 3.2 Routing and Connectivity

As one CRAM array is allocated to process each neuron, the basic connectivity between neurons directly translates into the connections between arrays to transfer spikes. Ideally, each neuron in SNN would be connected to all of the other neurons. However, such a fully connected scheme requires  $\binom{N}{2}$  connections between neurons, which is not feasible in hardware when the number of neurons is very high (i.e., in the order of Billions), due to the limited area. In order to eliminate the connectivity burden, a possible solution is using a 2-dimensional network as implemented in [6, 12, 17]. In [12], the 2-dimensional topology is further extended to a 3-dimensional Torus alongside additional diagonal connections and emergency routes. Such implementations involve each spike event to be transmitted as a packet in the mesh. This and similar solutions with more involved networks are subject to congestion in the packet traffic, eventually leading to packet drops.

Instead, we propose to use the Generalized De Bruijn Graph (GDBG) topology [7] to connect CRAM arrays. GDBG has been used in High Performance Computing and it is shown to be the near-optimal for load-balanced networks [10]. The

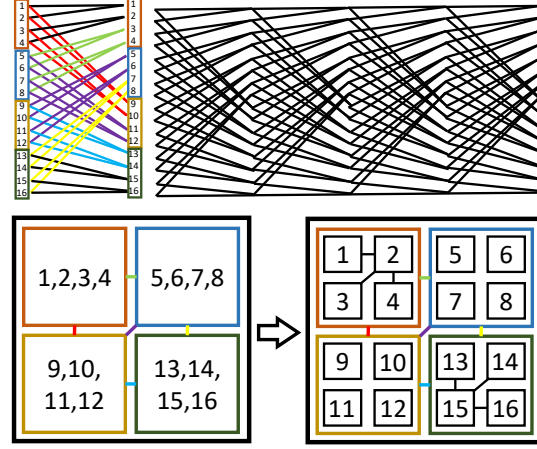


Fig. 5. Generalized De Bruijn Graph for an example 16-array network, self connections are not shown.

first advantage of GDBG is that each vertex has four edges at most, which is comparable to a 2-dimensional mesh. However, the connected vertices are not necessarily in the neighborhood of each other, which is defined in a lexicographical ordering sense. The second advantage is that the shortest path between any two vertices is  $\log_2 N$  for a graph with  $N$  vertices.

Since the connection pattern in GDBG is fixed, we can think about it as the same repeated pattern allowing each neuron to be connected to all other neurons in  $\log_2 N$  steps. Figure 5 depicts an example connection scheme for 16 neurons (labeled with numbers 1-16). in upper-left. When the connection scheme is expanded to  $\log_2 16 = 4$  time steps, we obtain the FFT-like diagram in upper-right. Indeed, this connectivity scheme is similar to Singleton’s FFT [22], which has a repetitive fixed pattern for each FFT *stage*, i.e., a set of operations with no internal data dependency. The upper-left portion of Figure 5 shows the resulting hierarchical architecture, where neurons are grouped in subsets of 4, as indicated with colored borders. The bottom portion of Figure 5 visualizes such an implementation where each edge corresponds to sets of wires between neurons. We have the connections between 4-neuron subsets on the bottom-left; and each neuron and its connections within the subset, on bottom-right. Applying such a quadtree decomposition, it is possible to map any  $N$ -neuron network in  $\log_4 N$  steps.

In our design, each CRAM array, which corresponds to a neuron, is connected to one another in GDBG topology. Each connection consists of  $j$  wires, which is equal to the maximum number of presynaptic neurons. Once the computation is done, the routing operations are initiated. The routing consists of  $\log_2 N$  stages. If the current stage  $c \in [1, \log_2 N]$  is smaller or equal to the number of presynaptic neurons  $j$ , then each array (i.e., neuron) concatenates the input spike trains and transmits them to the connected arrays for the next stage. This operation involves only reading incoming spike trains and writing them in the predetermined locations. Therefore no extra logic is involved if  $c \leq \log_2 j$ . However, if  $c > \log_2 j$ , each array combines the input spike trains using stored address values. Each array therefore reads  $\log_2 j$ -bit address values for each spike and copies the spike train to the corresponding addresses. Hence, upon initialization, each array has to store  $(\log_2 j)(\log_2 N - \log_2 j)$  bits of address values. After routing is complete, the next spike computation starts, as discussed in Section 3.1.

Fig. 6 demonstrates 4 routing stages of an example 16-neuron architecture, i.e.,  $j = 8$  and  $N = 16$ . In Stage 1 ( $c = 1$ ), the two spikes (highlighted in green and blue) coming from two neurons are combined and transmitted. In Stage 2 ( $c = 2$ ), the



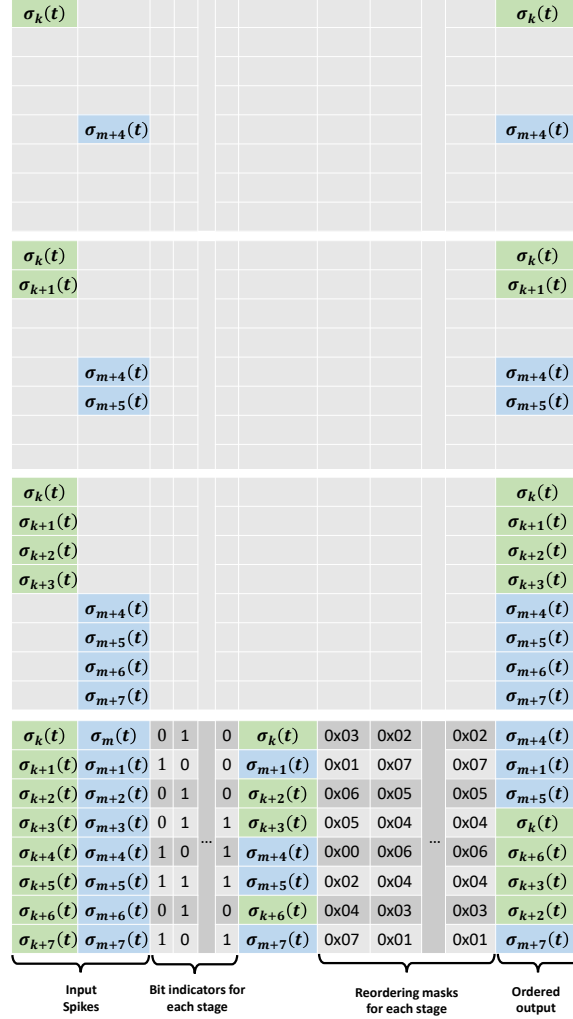


Fig. 6. Routing stages for an example 16-neuron (-array) architecture with maximum 8 presynaptic spikes.

number of incoming spikes doubles and combined spikes are forwarded to Stage 3. When  $c = 3$ , each incoming spike train has a size of four, and they are forwarded to the next stage. In Stage 4, however,  $c = 4$  is greater than  $\log_2 j = 3$  so half of the incoming spike trains should be discarded and the remaining spikes should be forwarded. For this purpose, we use a bit indicator for each stage, as shown in Figure 6. The bit indicators select one of the input spikes (highlighted in green and blue). The selected input spike train is read and then written to the ordered output in the corresponding address specified in the current stage's reordering (bit)mask. For this example, there is only one set of reordering masks and bit indicators, however, in general there can be  $\log_2 N - \log_2 j$  different sets of  $(\log_2 j)$ -bit masks and bit indicator sets.

*Our GDBG based design is efficient since we need  $2N$  connections for  $N$  neurons instead of  $\binom{N}{2}$ ; we avoid traffic handling which is required to implement NoC based architectures; and we can synchronize the whole system in deterministic time as each routing cycle entails a fixed amount of routing steps, which is  $\log_2 N$  for  $N$  neurons.*

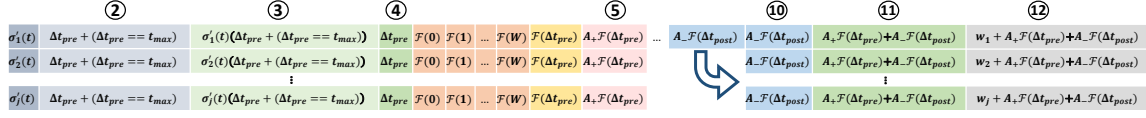


Fig. 7. Data layout for STDP engine in CRAM (transposed).

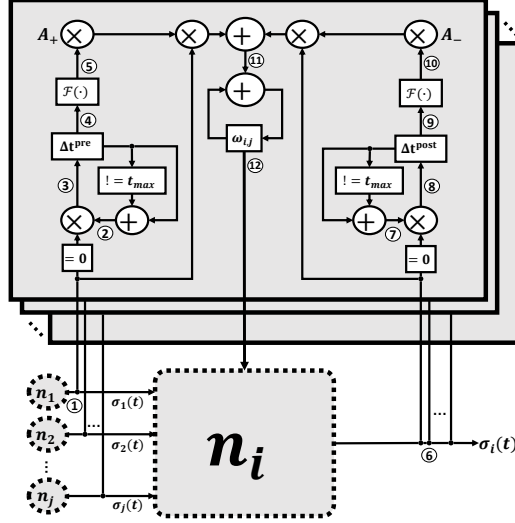


Fig. 8. Basic STDP diagram.

### 3.3 STDP Learning Engine

**3.3.1 Initialization.** Initialization steps for the STDP engine are similar to the feedforward case (Section 3.1.1). Note that  $\mathcal{F}(\cdot)$  is only a scaled version of  $\alpha_u(t)$  (Table 1). Therefore we re-use the lookup table for  $\alpha_u$  and scale any fetched value from it by multiplying the fetched value with  $\frac{1}{\tau_u}$ . We also initialize all parameters and constants from Equation 3 such  $A_{\pm}$ .

**3.3.2 Data flow.** In STDP engine, every time spike distribution is completed, presynaptic (postsynaptic) part of the operations is executed, as shown in the left (right) half in Figure 8, where the input is the spikes and the output is the weight. This effectively performs Equation (3). Note that the data dependency on presynaptic and postsynaptic spikes does not induce additional memory accesses since they are already stored in the same array in our mapping from Section 3.1. In the transposed layout, ① corresponds to the presynaptic spikes. ② is the incremented time difference since the arrival of the latest presynaptic spike and ③ resets the  $\Delta t^{pre}$  if the input neuron spikes. Then ⑤ is obtained by a lookup table implementation of  $\mathcal{F}(\cdot)$  function which is fed by ④. These steps are similar for ⑦, ⑧, ⑨, and ⑩ except that these calculations are only performed in one row and the output is copied to all rows as shown in the layout in Figure 7. Finally,  $\Delta\omega$  is added to  $\omega$  as shown in ⑪ and ⑫.

**3.3.3 Low level operations.** Addition and multiplication operations in the STDP are similar to the feedforward case as discussed in Section 3.1.3. Comparators are implemented using a cascade of AND gates.

#### 4 EVALUATION

In order to evaluate our design, we perform energy and performance analysis based on the low level elementary operations such as Boolean gate implementations in the context of the proposed CRAM-based SNN architecture. Configuration parameters for the simulations are given in Table 3. For experiments, we have four different configurations where STT-M and SHE-M correspond to the current conservative estimates while STT-F and SHE-F reflect near-term future expectations for STT and SHE based MTJs. For array characteristics such as read/write timing, we use NVSim [9]. Each array has an *array controller* which is responsible for driving logic lines, bitlines, and wordlines. We take the overhead resulting from driving such lines into consideration. For synaptic events, we stick to a conservative set-up where each presynaptic neuron spikes in each time step and each neuron is connected to the maximum possible number of neurons. Since we base our neuron model on Loihi’s implementation, we compare our results with the energy and time figures reported in [6] and [16], using  $L = 1024$  and  $F = 1024$  for 1-bit synaptic weights (in their design,  $L$  is the neuron count per core;  $F$ , the postsynaptic fanout).

Table 3. Configuration Parameters

Parameter	STT-M, SHE-M	STT-F, SHE-F
P state resistance	3.15 k $\Omega$	7.34 k $\Omega$
AP state resistance	7.34 k $\Omega$	76.39 k $\Omega$
Switching Time	3 ns	1 ns
Switching Current	40 $\mu$ A	3 $\mu$ A
Bulk preset current limit	30 mA	

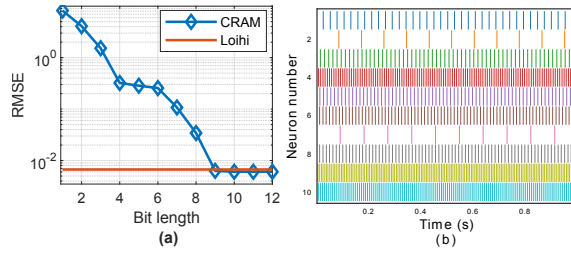


Fig. 9. (a) RMSE vs.  $\log_2 L_f$  bit length for an example 10-neuron CRAM-SNN compared to 9-bit Loihi. (b) The spike-time diagram.

For accuracy analysis, we use Loihi library of Nengo framework [1] with Loihi configuration. Modifying Nengo Loihi’s implementation, we analyze the spiking accuracy for our lookup table based limited precision design. This analysis is only used for Leaky Integrate-and-Fire feedforward implementation. As shown in Figure 9, RMSE error is comparable to Loihi if at least 9 bits are allocated for each lookup table entry. Although the accuracy loss is significant in higher bit lengths, Figure 9 (a) shows that a similar bit length to Loihi implementation provides similar accuracy to Loihi. Figure 9 (b) features 10-neuron spike-time diagram used for the analysis.

Table 4 summarizes the results for 1 Billion neurons, where the maximum number of presynaptic neurons is 1024, bit length is 1 and the filter (lookup table) size is 64. Each CRAM array has 1024 $\times$  512 cells.

It can be seen that although all CRAM configurations can provide enough performance to implement SNN operations within a biologically plausible time budget, i.e., a spiking rate of several kHz, SHE-F configuration provides the lowest energy consumption and fastest operation.

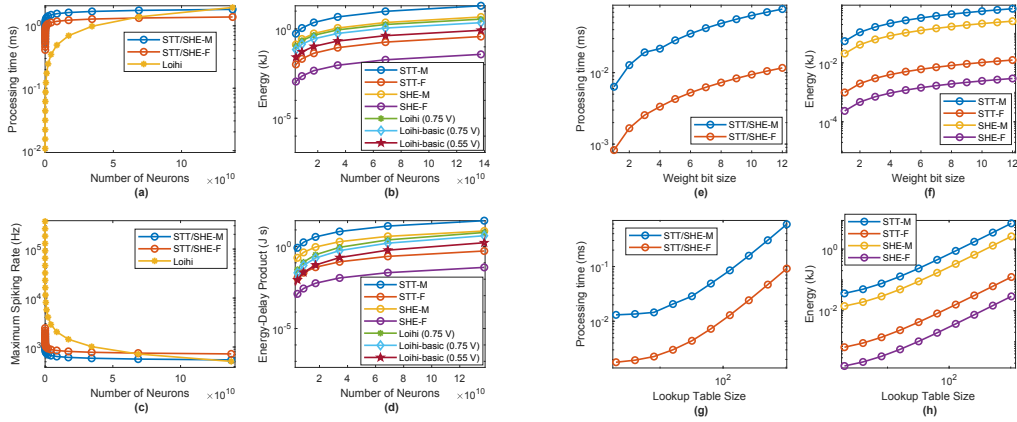
Fig. 10. Sensitivity to number of neurons, weight bit length and  $\alpha_u$  table size.

Table 4. Evaluation Results

Metric	STT-M	STT-F	SHE-M	SHE-F
Execution Time ( $\mu$ s)	6.342	0.825	6.342	0.825
Maximum Spiking Rate (KHz)	157.7	1212.3	157.7	1212.3
Energy (J)	54.51	0.989	20.61	0.234
EDP ( $\mu$ Js)	345.72	0.816	130.74	0.193

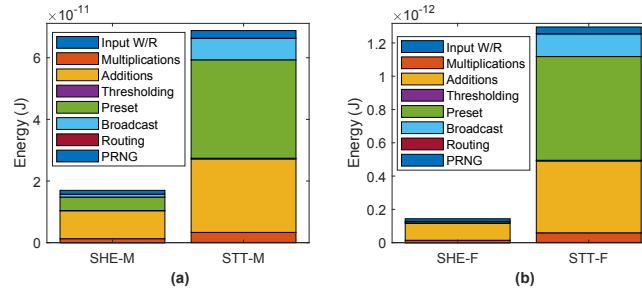


Fig. 11. Overall energy breakdown of operations in a single instance of spiking events.

Figure 11 shows the energy breakdown for a single spike operation with 1 bit weights. We observe that preset and additions dominate the overall energy followed by multiplication (i.e., AND) operations, pointing to further hardware optimization opportunities.

Figure 10 shows execution time, maximum spiking rate, energy and energy-delay-product (EDP) for the case where maximum number of presynaptic neurons is 1024 and the bit length is 8. Figure 10(a) and 10(c) are complementary figures for -M and -F variants compared to Loihi model for similar parameters. Although Loihi is faster for larger number of neurons because of its faster computation, CRAM variants surpass Loihi when neuron count approaches to hundred billions thanks to our routing architecture. Figure 10(b) and 10(d) capture energy and EDP's sensitivity to neuron counts in several Loihi models with different voltages. For very large neuron counts, the best performing CRAM variants have lower energy

consumption than Loihi, and higher energy efficiency. We also sweep bit length of weights and table size for  $\alpha_u$ , as shown in Figure 10(e)–(h). Figures 10(e) and 10(f) show processing time and energy consumption for different weight bit lengths; and Figures 10(g) and 10(h) capture the processing time and energy for various lookup table sizes in the feedforward design. In all cases, STT/SHE-F or SHE-F configuration provide the lowest processing time and energy when compared to other CRAM variants, emphasizing the effect of the cell technology.

Overall, when compared to the best performing Loihi baseline (0.55V) with a fanout of 1024, and 1-bit synaptic weights, SHE-F configuration consumes 26.13× less energy. At the same time, SHE-F is 3.99× more energy efficient (in terms of EDP, energy-delay-product) for the feedforward implementation as captured in Figure 10.

Table 5. Energy, latency, and EDP for single spike operation.

Synaptic Parameter	SHE-F	Loihi
Spike Operation Energy	143.81 fJ	23.6 pJ
Spike Operation Time	499.86 ns	3.5 ns
Spike Operation EDP	7.19e-20 Js	8.26 e-20 Js
STDP Update Energy	0.33 pJ	120 pJ
STDP Update Time	1321.7 ns	6.1 ns
STDP Update EDP	4.38e-19 Js	7.32 e-19 Js

Table 5 summarizes low level performance parameters of our best case CRAM-SNN design for 1-bit weights where  $L_f = 32$  for feedforward computations. Also tabulated are Loihi’s corresponding low-level performance parameters for comparison. STDP operations are performed at 10-bit precision.  $L_f = 32$  is chosen to capture enough accuracy to model  $\alpha_u(t)$  while lowering logic complexity to maintain a low energy consumption. 10-bit precision suffices to provide enough bandwidth for updating up to 9 bit weights, which is meaningful for a fair comparison. Although being slower, our design consumes significantly less energy, which leads to a lower EDP for a single spike operation with a single presynaptic connection for 1 bit weights.

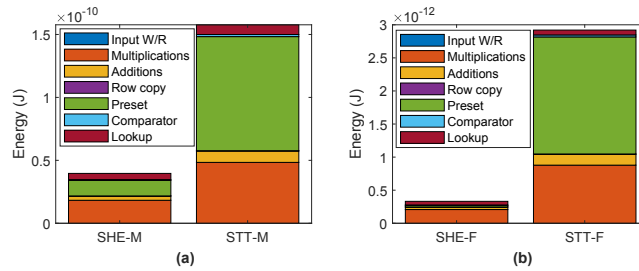


Fig. 12. Single-spike energy breakdown of STDP weight update operation.

Figures 13(a) and 13(b) show the STDP processing time and energy for larger bit lengths. Processing times in 13(a) irregularly increase around 6-bits as CRAM preset operations become overwhelming, however, this does not effect the energy consumption pattern in 13(b) where the SHE-F configuration outperforms the other CRAM variants. Energy breakdown of STDP operations are given in Figures 12(a) and 12(b). Similar to the feedforward case, energy consumption is mostly dominated by preset, addition and multiplication operations in STDP weight update. Low level performance results further show that our gains are not only due to the proposed connectivity scheme, but also because of the low energy, massively parallel logic operations CRAM enables.

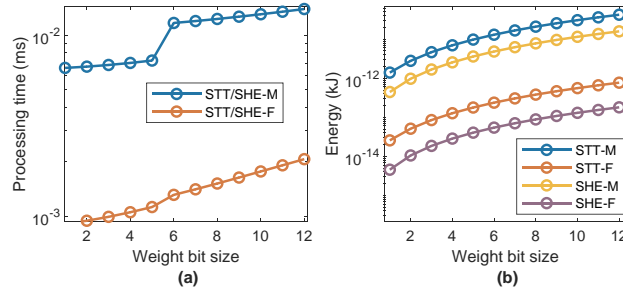


Fig. 13. (a) Processing time vs. weight bit length. (b) STDP update energy vs. weight bit length.

## 5 CONCLUSION

We introduce a CRAM-based SNN architecture, where each neuron is processed inside a single CRAM array while the arrays are connected to each other in a GDBG topology. We thereby achieve a limited full connectivity by using only  $2N$  connections in a  $N$  neuron network, instead of  $\binom{N}{2}$ , while exploiting the massive intra- and inter-array parallelism and energy efficiency of CRAM for logic operations. Our best configuration results in  $164.1\times$  less energy consumption and similar EDP for feedforward operations; and  $361.77\times$  less energy consumption and  $1.66\times$  lower EDP for learning (via STDP) when compared to the alternative Loihi architecture.

## REFERENCES

- [1] Trevor Bekolay, James Bergstra, Eric Hunsberger, Travis DeWolf, Terrence C Stewart, Daniel Rasmussen, Xuan Choo, Aaron Voelker, and Chris Eliasmith. 2014. Nengo: a Python tool for building large-scale functional brain models. *Frontiers in neuroinformatics* 7 (2014), 48.
- [2] Mei-Chin Chen, Abhronil Sengupta, and Kaushik Roy. 2018. Magnetic skyrmion as a spintronic deep learning spiking neuron processor. *IEEE Transactions on Magnetics* 54, 8 (2018), 1–7.
- [3] Z. Chowdhury, J. D. Harms, S. K. Khatamifard, M. Zabihi, Y. Lv, A. P. Lyle, S. S. Sapatnekar, U. R. Karpuzcu, and J. Wang. 2018. Efficient In-Memory Processing Using Spintronics. *IEEE Computer Architecture Letters* 17, 1 (Jan 2018), 42–46. DOI: <http://dx.doi.org/10.1109/LCA.2017.2751042>
- [4] Z. I. Chowdhury, S. K. Khatamifard, Z. Zhao, M. Zabihi, S. Resch, M. Razaviyayn, J. Wang, S. Sapatnekar, and U. R. Karpuzcu. 2019. Spintronic In-Memory Pattern Matching Using Computational RAM (CRAM). *IEEE Journal on Exploratory Solid-State Computational Devices and Circuits* (2019), 1–1. DOI: <http://dx.doi.org/10.1109/JXCDC.2019.2951157>
- [5] Khanh N Dang and Abderazek Ben Abdallah. 2019. An Efficient Software-Hardware Design Framework for Spiking Neural Network Systems. *2019 International Conference on Internet of Things, Embedded Systems and Communications (IIINTEC)* (2019).
- [6] Mike Davies, Narayan Srinivasa, Tsung-Han Lin, Gautham Chinya, Yongqiang Cao, Sri Harsha Choday, Georgios Dimou, Prasad Joshi, Nabil Imam, Shweta Jain, and others. 2018. Loihi: A neuromorphic manycore processor with on-chip learning. *IEEE Micro* 38, 1 (2018), 82–99.
- [7] N. G. DE BRUIJN. 1946. A combinatorial problem. *Proc. Koninklijke Nederlandse Academie van Wetenschappen* 49 (1946), 758–764. <https://ci.nii.ac.jp/naid/10019660672/en/>
- [8] Julie Dethier, Paul Nuyujukian, Chris Eliasmith, Terrence C Stewart, Shaqui A Elasaad, Krishna V Shenoy, and Kwabena A Boahen. 2011. A brain-machine interface operating with a real-time spiking neural network control algorithm. In *Advances in neural information processing systems*. 2213–2221.
- [9] X. Dong, C. Xu, Y. Xie, and N. P. Jouppi. 2012. NVSim: A Circuit-Level Performance, Energy, and Area Model for Emerging Nonvolatile Memory. *IEEE Transactions on Computer-Aided Design of Integrated Circuits and Systems* 31, 7 (July 2012), 994–1007. DOI: <http://dx.doi.org/10.1109/TCAD.2012.2185930>
- [10] P. Faizian, M. A. Mollah, X. Yuan, Z. Alzaid, S. Pakin, and M. Lang. 2018. Random Regular Graph and Generalized De Bruijn Graph with  $k$ -Shortest Path Routing. *IEEE Transactions on Parallel and Distributed Systems* 29, 1 (Jan 2018), 144–155. DOI: <http://dx.doi.org/10.1109/TPDS.2017.2741492>
- [11] Charlotte Frenkel, Martin Lefebvre, Jean-Didier Legat, and David Bol. 2018. A 0.086-mm<sup>2</sup> 12.7-pJ/SOP 64k-synapse 256-neuron online-learning digital spiking neuromorphic processor in 28-nm CMOS. *IEEE transactions on biomedical circuits and systems* 13, 1 (2018), 145–158.
- [12] Steve B Furber, Francesco Galluppi, Steve Temple, and Luis A Plana. 2014. The spinnaker project. *Proc. IEEE* 102, 5 (2014), 652–665.
- [13] Xin Jin, Mikel Lujan, Luis A Plana, Sergio Davies, Steve Temple, and Steve B Furber. 2010. Modeling spiking neural networks on SpiNNaker. *Computing in science & engineering* 12, 5 (2010), 91–97.
- [14] Dayeol Lee, Gwangmu Lee, Dongup Kwon, Sunghwa Lee, Youngsok Kim, and Jangwoo Kim. 2018. Flexon: a flexible digital neuron for efficient spiking neural network simulations. In *2018 ACM/IEEE 45th Annual International Symposium on Computer Architecture (ISCA)*. IEEE, 275–288.

- [15] Roberto Lent, Frederico AC Azevedo, Carlos H Andrade-Moraes, and Ana VO Pinto. 2012. How many neurons do you have? Some dogmas of quantitative neuroscience under revision. *European Journal of Neuroscience* 35, 1 (2012), 1–9.
- [16] Andrew Lines, Prasad Joshi, Ruokun Liu, Steve McCoy, Jonathan Tse, Yi-Hsin Weng, and Mike Davies. 2018. Loihi asynchronous neuromorphic research chip. In *2018 24th IEEE International Symposium on Asynchronous Circuits and Systems (ASYNC)*. IEEE, 32–33.
- [17] Paul A Merolla, John V Arthur, Rodrigo Alvarez-Icaza, Andrew S Cassidy, Jun Sawada, Filipp Akopyan, Bryan L Jackson, Nabil Imam, Chen Guo, Yutaka Nakamura, and others. 2014. A million spiking-neuron integrated circuit with a scalable communication network and interface. *Science* 345, 6197 (2014), 668–673.
- [18] D. E. Nikonov and I. A. Young. 2019. Benchmarking Delay and Energy of Neural Inference Circuits. *IEEE Journal on Exploratory Solid-State Computational Devices and Circuits* 5, 2 (2019), 75–84.
- [19] Salonik Resch, S. Karen Khatamifard, Zamshed Iqbal Chowdhury, Masoud Zabihi, Zhengyang Zhao, Jian-Ping Wang, Sachin S. Sapatnekar, and Ulya R. Karpuzcu. 2019. PIMBALL: Binary Neural Networks in Spintronic Memory. *ACM Trans. Archit. Code Optim.* 16, 4, Article 41 (Oct. 2019), 26 pages. DOI: <http://dx.doi.org/10.1145/3357250>
- [20] S. Schmitt, J. KlÄdhn, G. Bellec, A. GrÄijbl, M. GÄijttler, A. Hartel, S. Hartmann, D. Husmann, K. Husmann, S. Jeltsch, V. Karasenko, M. Kleider, C. Koke, A. Kononov, C. Mauch, E. MÄijller, P. MÄijller, J. Partzsch, M. A. Petrovici, S. Schiefer, S. Scholze, V. Thanasoulis, B. Vogginger, R. Legenstein, W. Maass, C. Mayr, R. SchÄijffny, J. Schemmel, and K. Meier. 2017. Neuromorphic hardware in the loop: Training a deep spiking network on the BrainScaleS wafer-scale system. In *2017 International Joint Conference on Neural Networks (IJCNN)*. 2227–2234. DOI: <http://dx.doi.org/10.1109/IJCNN.2017.7966125>
- [21] Abhronil Sengupta, Aparajita Banerjee, and Kaushik Roy. 2016. Hybrid spintronic-CMOS spiking neural network with on-chip learning: Devices, circuits, and systems. *Physical Review Applied* 6, 6 (2016), 064003.
- [22] R Singleton. 1967. A method for computing the fast Fourier transform with auxiliary memory and limited high-speed storage. *IEEE Tran. on Audio and Electroacoustics* 15, 2 (1967).
- [23] Terrence Stewart, Feng-Xuan Choo, and Chris Eliasmith. 2012. Spaun: A perception-cognition-action model using spiking neurons. In *Proceedings of the Annual Meeting of the Cognitive Science Society*, Vol. 34.
- [24] Evangelos Stomatias, Miguel Soto, Teresa Serrano-Gotarredona, and Bernabé Linares-Barranco. 2017. An event-driven classifier for spiking neural networks fed with synthetic or dynamic vision sensor data. *Frontiers in neuroscience* 11 (2017), 350.
- [25] E. I. Vatajelu and L. Anghel. 2017. Fully-connected single-layer STT-MTJ-based spiking neural network under process variability. In *2017 IEEE/ACM International Symposium on Nanoscale Architectures (NANOARCH)*. 21–26. DOI: <http://dx.doi.org/10.1109/NANOARCH.2017.8053727>
- [26] Jian-Ping Wang and Jonathan D Harms. 2015. General structure for computational random access memory (CRAM). (Dec. 29 2015). US Patent 9,224,447.
- [27] Kezhou Yang, Akul Malhotra, Sen Lu, and Abhronil Sengupta. 2020. All-Spin Bayesian Neural Networks. *IEEE Transactions on Electron Devices* 67, 3 (2020), 1340–1347.
- [28] Shihui Yin, Deepak Kadetotad, Bonan Yan, Chang Song, Yiran Chen, Chaitali Chakrabarti, and Jae-sun Seo. 2017. Low-power neuromorphic speech recognition engine with coarse-grain sparsity. In *2017 22nd Asia and South Pacific Design Automation Conference (ASP-DAC)*. IEEE, 111–114.
- [29] M. Zabihi, Z. I. Chowdhury, Z. Zhao, U. R. Karpuzcu, J. Wang, and S. S. Sapatnekar. 2019. In-Memory Processing on the Spintronic CRAM: From Hardware Design to Application Mapping. *IEEE Trans. Comput.* 68, 8 (Aug 2019), 1159–1173. DOI: <http://dx.doi.org/10.1109/TC.2018.2858251>
- [30] M. Zabihi, Z. Zhao, D. Mahendra, Z. I. Chowdhury, S. Resch, T. Peterson, U. R. Karpuzcu, J. Wang, and S. S. Sapatnekar. 2019. Using Spin-Hall MTJs to Build an Energy-Efficient In-memory Computation Platform. In *20th International Symposium on Quality Electronic Design (ISQED)*. 52–57. DOI: <http://dx.doi.org/10.1109/ISQED.2019.8697377>
- [31] Deming Zhang, Lang Zeng, Youguang Zhang, Weisheng Zhao, and Jacques Olivier Klein. 2016. Stochastic spintronic device based synapses and spiking neurons for neuromorphic computation. In *2016 IEEE/ACM International Symposium on Nanoscale Architectures (NANOARCH)*. IEEE, 173–178.